1  **Could the two anticyclonic eddies during winter 2003/2004 be reproduced and**

2  **predicted in the northern south China sea?**

4  Dazhi Xu [1,3], Wei Zhuang[4], Youfang Yan [2*]

6  [1]South China Sea Marine Prediction Center, State Oceanic Administration, Guangzhou, China

7  [2]South China Sea Institute of Oceanology, Chinese Academic of Science, Guangzhou, China

8  [3]Nansen Environmental and Remote Sensing Center, Bergen, Norway

9  [4]State Key Laboratory of Marine Environmental Science & College of Ocean and Earth

10  Sciences, Xiamen University, Xiamen 361102, China

11                                    **Abstract**

12    Great progress has been made in understanding the mesoscale eddies and their role on

13    the large-scale structure and circulation of the oceans. However, many questions still

14    remain to be resolved, especially with regard to the reproductivity and predictability of

15    mesoscale eddies. In this study, the reproductivity and predictability of mesoscale

16    eddies in the Northern SCS (NSCS), a region with strong eddy activity, are investigated

17    with a focus on two typical anticyclonic eddies (AE1 and AE2) based on a HYCOM-

18    EnOI Assimilated System. The comparisons of assimilated results and observations

19    suggest that generation, evolution and propagation paths of AE1 and AE2 can be well

20    reproduced and forecasted when the observed amplitude >8 cm (or the advective

21    nonlinearity parameter U/c greater than 2), although their forcing mechanisms are quite

22    different. However, when their amplitudes are less than 8 cm, the generation and decay

23    of these two mesoscale eddies cannot be well reproduced and predicted by the system.

24    This result suggests, in addition to dynamical mechanisms, the spatial resolution of

25    assimilation observation data and numerical models must be taken into account in

26    reproducing and predicting mesoscale eddies in the NSCS.

28    **Keywords:** HYCOM; EnOI; Northern South China Sea; Mesoscale eddy;

29    Predictability

## 1. Introduction

Equivalent to the synoptic variability of the atmosphere, ocean mesoscale eddies are often described as the "weather" of the ocean, with typical spatial scales of ~100 km and time scales of a month (Wang et al., 1996; Liu et al., 2001; Chelton et al., 2011). The mesoscale eddy is characterized by temperature and salinity anomalies with associated flow anomalies, exhibiting different properties to their surroundings, thus allowing them to control the strength of mean currents and to transport heat, salt, and biogeochemical tracers around the ocean. The motion of mesoscale eddies would be a straight line, if eddies freely propagate in open ocean. However, most of eddies may have interaction with topography, strong currents (western boundary current), eddies during their lifetime. The motion of eddy will be modified and even split when approaching an island (Yang et al., 2017). It is also recognized that western boundary is graveyard of eddies (Zhai et al., 2010). The dynamical processes such as splitting and/or merging of eddies can also make termination and/or genesis of eddies in open ocean (Li et al., 2016). Thus, the dynamical processes make that the prediction of eddy motion is a challenge for ocean simulation. Although today, the beauty and complexity, the scales resolved, the eddy energy and tracking and the effects on atmosphere of these mesoscale features can be seen by viewing high resolution satellite images or numerical model simulations (Yang et al., 2000; Fu et al., 2010; Morrow and Le Traon, 2012; Frenger et al., 2013), the operational forecasts of the mesoscale eddy still pose a big challenge because of its complicated dynamical mechanisms and high nonlinearity (Woodham et al., 2015; Treguier et al., 2017; Vos et al., 2018). A recent example is the

52 explosion of the Deepwater Horizon drilling platform in the northern Gulf of Mexico

53 in 2010 where an accurate prediction of the position and propagation of the Loop

54 Current eddy was essential in determining if the spilled oil would be advected to the

55 Atlantic Ocean or still remain within the Gulf (Treguier et al., 2017).

56 Similar to Gulf of Mexico, the South China Sea (SCS) is also a large semi-closed

57 marginal sea in the northwest Pacific, connecting to the western Pacific through the

58 Luzon Strait (Fig. 1). Forced by seasonal monsoon winds, the intrusion of Kuroshio

59 Current (KC), the Rossby waves and the complex topography, the SCS, especially the

60 Northern SCS (NSCS) exhibits significant mesoscale eddy activity (Fig. 2). Many

61 studies have tried to investigate mesoscale eddies in the NSCS (Wang et al., 2003; Jia

62 et al., 2005; Wang et al., 2008). Based on the potential vorticity conservation equation

63 and in-situ survey data, Yuan and Wang (1986) pointed out that the bottom topography

64 forcing might be the primary factor for the formation of anticyclonic eddies in the

65 northeast of Dongsha Islands (DIs). Using survey CTD data in September 1994, Li et

66 al. (1998) recorded evidence of anticyclonic eddies in the NSCS and suggested these

67 anticyclonic eddies are probably shed from the KC. Investigations by Wu et al. (2007)

68 showed that westward propagating eddies in the NSCS originate near the Luzon Strait

69 rather than coming from the western Pacific. Based on the altimeter, the trajectory of

70 drift and the hydrological observations data, Wang et al. (2008) studied the evolution

71 and migration of two anticyclonic eddies in the NSCS during winter of 2003/2004. As

72 they described, the AE1 generated by interaction of the unstable rotating fluid with the

73 sharp topography of DIs firstly appeared near DIs on the 10th of December 2003 (see

74  Fig. 3). Then it began to move southwestward with its amplitude decreasing gradually.

75  During the movement of AE1, another anticyclonic eddy (AE2) was shed and

76  developed from the loop current of Kuroshio near the Luzon Strait on the 14th of January

77  2004. The amplitude of AE2 was then increased when it propagated southwestward

78  (Fig. 3d-3f). About five weeks later, AE2 reached its maximum in amplitude and then

79  lasted around three weeks in its mature state. During its decay phase, AE2 moved

80  southwestward quickly with its amplitude decreasing, and finally disappeared at the

81  location of 114°E, 18°N on the 7th of April 2004. Meanwhile, AE1 continued moving

82  to southwest and eventually disappeared southeast of Hainan. In addition to physical

83  characteristics, the phytoplankton community at these two eddies have also been

84  studied by Huang et al. (2010). These studies improved our understanding of activities

85  of mesoscale eddy and its possible dynamical mechanisms in the NSCS.

86      Despite the activities and its possible dynamical mechanisms of mesoscale eddies

87  in the NSCS having received much attention in past decades, studies on the

88  reproductivity and predictability of mesoscale eddies in the NSCS are still rare. As

89  mentioned above, mesoscale eddies are not only related to complicated dynamical

90  mechanisms but also involve strong nonlinear processes (Oey et al., 2005); they are not

91  a deterministic response to atmospheric forcing. The quality of mesoscale eddies

92  forecasting will depend primarily on the quality of the initial conditions. Ocean data

93  assimilation, which combines observations with the numerical model, can provide more

94  realistic initial conditions and thus is essential for the prediction of mesoscale eddies.

95  As shown by previous studies, after assimilating altimeter data into ocean models, the

96    ocean currents in the southern SCS (Xiao et al., 2006) and the realism of three largest

97    eddies in the SCS appear during Typhoon Rammasun (Xie et al., 2018) have been

98    improved. Furthermore, some studies show that the ocean model includes tides or

99    assimilated altimeter data with reasonable MDT, can provide more realistic initial

100   conditions (Xie et al., 2011; Xu et al., 2012). The above studies show that the mesoscale

101   eddies in the SCS are reproducible, but about the predictability of mesoscale eddies is

102   rare. In this study, we assessed the reproduction and predictability of two typical

103   anticyclonic eddies (Wang et al., 2008), owing to be represented different generation

104   mechanisms and survive long enough to be useful, in the NSCS with focus on their

105   generation, evolution and decay processes by a series of numerical experiments based

106   on a Chinese Shelf/Coastal Seas Assimilation System (CSCASS; Li, 2009; Li et al.,

107   2010; Zhu, 2011) along with the observation data from surface drifter trajectory and

108   satellite remote sensing.

109   **2. Datasets and Methodologies**

110   **2.1 Datasets**

111       In this study, the altimetric data between 2003-2004, which includes along-track

112   SLA, totally 29 passes (about 9300 points) over the domain of CSCS was selected.

113   Considering the noise of SLA measurement in the shallow seas, data for the shallow

114   areas with depth<400 m was excluded. In order to verify, the merged SLA based on

115   Jason-1, TOPEX/Poseidon, ERS-2 and ENVISAT (Ducet et al., 2000) provided by

116   Archiving, Validation and Interpretation of Satellites Oceanographic data (AVISO) at

117     Centre Localization Satellite (CLS, ftp://ftp.aviso.oceanobs.com/global/nrt/) with 1/4°

118     x 1/4° resolution and weekly average are used. In addition, because the SLA present

119     only the anomalies relative to a time-mean sea level field, thus a new mean dynamic

120     topography (nMDT), which has been corrected using iterative method by Xu et al.

121     (2012) was used to calculate the realistic sea level in this study.

122     In addition to SLA datasets, the daily OISST from the National Oceanic and

123     Atmospheric Administration's (NOAA) National Climatic Data Center

124     (ftp://eclipse.ncdc.noaa.gov/pub/OI-daily-v2/NetCDF/), which was merged by an

125     optimum interpolation method (Reynolds et al., 2007) based on the Infrared SST

126     collected by the Advanced Very High Resolution Radiometer sensors on the NOAA

127     Polar Orbiting Environmental Satellite and SST from Advanced Microwave Scanning

128     Radiometer for the Earth Observing System, are also used. The daily OISST's biases

129     were fixed using in situ data from ships and buoys. The dataset between 2003 and 2004

130     was used in this study, with a spatial resolution of $1/4° \times 1/4°$. In addition, the surface

131     drifting buoy data from the World Ocean Circulation Experiment (WOCE,

132     ftp://ftp.aoml.noaa.gov/pub/phod/buoydata/) are also used. Three drifters were

133     designed to drift at the surface within the upper 15 m and tracked by the ARGOS

134     satellite system. Positions of the drifters were smoothed using a Gaussian-filter scale of

135     24 h to eliminate tidal and inertial currents, and were subsampled at 6 h intervals

136     (Hamilton et al., 1999).

137     **2.2 Method of identify the mesoscale eddies**

138     Similar to the standard of Cheng et al. (2005) and Chelton et al. (2011), we identify

139  the mesoscale eddies in this study as follows: 1) there must be a closed contour on the

140  merged SLA; 2) there must be one maximum or minimum inside the area of the closed

141  contour for anticyclonic or cyclonic eddy; 3) the difference between the extremum and

142  the outermost closed SLA contour, that is, the amplitude of the mesoscale eddy, must

143  be greater than 2 cm; and 4) the spatial scale of the eddy should be 45-500 km. In

144  addition, the amplitude (A) of an eddy is defined here to be the magnitude of the

145  difference between the estimated basal height of the eddy boundary and the extremum

146  value of SSH within the eddy interior: $A=|h_{ext}-h_0|$.

147  **2.3 Ocean model**

148  We here used a three-dimensional hybrid coordinate ocean model (HYCOM;

149  Halliwell et al., 1998; 2000; Bleck, 2002; Halliwell, 2004; Chassignet et al., 2007) to

150  provide a dynamical interpolator of observation data in the assimilation system.

151  HYCOM is a primitive equation general ocean circulation model with vertical

152  coordinates: isopycnic coordinate in the open stratified ocean, the geopotential (or z)

153  coordinate in the weakly stratified upper ocean, and the terrain following sigma-

154  coordinate in shallow coastal regions.

155  In this study, HYCOM was implemented in the Chinese shelf/coastal seas with a

156  horizontal resolution of $1/12°\times1/12°$, and in the remaining regions with $1/8°\times1/8°$, the

157  model domain is from 0°N to 53°N and from 99°E to 143°E, the detail model domain

158  and grid can refer to the inset panel of Fig.1. The vertical water column from the sea

159  surface to the bottom was divided into 22 levels. The K-Profile Parameterization (KPP;

160  Large et al., 1994), which has proved to be an efficient mixing parameterization in many

161  oceanic circulation models, was used here. The bathymetry data of the model domain

162  were taken from the 2-Minute Gridded Global Relief Data (ETOPO2).

163      To adjust the model dynamics and achieve a perpetually repeating seasonal cycle

164  before applying the interannual atmospheric forcing, the model was initialized with

165  climatological temperature and salinity from the World Ocean Atlas 2001 (WOA01;

166  Boyer et al., 2005) and was driven by the Comprehensive Ocean-Atmosphere Data Set

167  (COADS; Woodruff et al., 1987) in the spin-up stage. After integrating ten model years

168  with climatological forcing, the model was forced by the European Center for Medium-

169  Range Weather Forecasts (ECMWF) 6-hourly reanalysis dataset (Uppala et al., 2005)

170  from 1997 to 2003. The wind velocity (10-m) components were converted to stresses

171  using a stability dependent drag coefficient from Kara et al. (2002). Thermal forcing

172  included air temperature, relative humidity and radiation (shortwave and longwave)

173  fluxes. Precipitation was also used as a surface forcing from Legates and Willmott

174  (1990). Surface latent and sensible heat fluxes were calculated using bulk formulae

175  (Han, 1984). Monthly river runoff was parameterized as a surface precipitation flux in

176  the ECS, the SCS and Luzon Strait (LS) from the river discharge stations of the Global

177  Runoff Data Centre (GRDC) (http://www.bafg.de), and scaled as in Dai et al. (2002).

178  Temperature, salinity and currents at the open boundaries were provided by an India-

179  Pacific domain HYCOM simulation at $1/4° \times 1/4°$ spatial resolution (Yan et al., 2007).

180  Surface temperature and salinity were relaxed to climate on a time scale of 100 days.

181  Both two-dimensional barotropic fields such as Sea Surface Height and barotropic

182  velocities, and three-dimensional baroclinic fields such as currents, temperature,

183    salinity and density were stored daily.

184    **2.4 The assimilation scheme**

185        The ensemble optimal interpolation scheme (EnOI; Oke et al., 2002), which is

186    regarded as a simplified implementation of the Ensemble Kalman Filter (EnKF), aims

187    at alleviating the computational burden of the EnKF by using stationary ensembles to

188    propagate the observed information to the model space. The data assimilation schemes

189    can be briefly written as (Oke et al., 2010):

190    $$\vec{\psi}^a = \vec{\psi}^b + K(\vec{d} - H\vec{\psi}^b) \tag{1}$$

191    $$K = P^b H^T [HP^b H^T + R]^{-1} \tag{2}$$

192    where $\vec{\psi}$ is the model state vectors including model temperature, layer thickness and

193    velocity; Superscripts $a$ and $b$ denote analysis and background, respectively; $\vec{d}$ is

194    the measurement vector that consists of SST and SLA observations; $K$ is the gain

195    matrix; and $H$ is the measurement operator that transforms the model state to

196    observation space. $P$ is the background error covariance and $R$ is the measurement

197    error covariance. In EnOI, Eq. 2 can be expressed as:

198    $$K = \alpha(\sigma \circ P^b)H^T[\alpha H(\sigma \circ P^b)H^T + R]^{-1} \tag{3}$$

199    where α is a scalar that can tune the magnitude of the analysis increment; σ is a

200    correlation function for localization; and $P^b$ is the background error covariance which

201    can be estimated by

202    $$P^b = A' A'^T / (n - 1) \tag{4}$$

203    In Eq. 4, $n$ is the ensemble size, $A'$ is the anomaly of the ensemble matrix, $A =$

204 $(\psi_1, \psi_2, \cdots, \psi_N) \in \Re^{n \times N}$ $(\psi_i \in \Re^N (i = 1, \cdots, n)$ is the ensemble members, $N$ is the

205 dimension of the model state, representing usually the model variability at certain scales

206 by using a long-term model run or spin-up run. More detailed description and

207 evaluation of the CSCASS are in Li et al. (2010) and Xu et al. (2012).

208

209 **3. Results**

210 **3.1 The reproduction of anticyclonic eddies AE1 and AE2 in the NSCS**

211     In order to investigate whether the evolution and migration features of these two

212 eddies can be reproduced by the CSCASS or not, we firstly set up an assimilation

213 experiment named As_exp (see Fig. 4, black line) for AE1 and AE2. In this experiment,

214 the observed SST and SLA are both assimilated into CSCASS every 3 days. To meet

215 dynamic adjustment, the first assimilation was performed on the 27$^{th}$ of September 2003,

216 two months prior to the generation of AE1.

217     Base on the As_exp experiment output, we use the observations SLA to evaluate

218 the uncertainty of CSCASS in the research area. In this study, we calculated the weekly

219 mean RMS error (RMSE) of the As_exp /control experiments output and observations

220 for SLA. As the result indicates, the RMSE for the As_exp is between 6 cm to 14 cm,

221 while RMSE for the control is between 10 cm to 18 cm. This result suggested that data

222 assimilation improved effectively the SLA field and had a beneficial impact on model

223 results in this area.

224     In addition, we also use the Advective Nonlinearity Parameter U/c (ANP, Chelton

225 et al., 2011; Li et al., 2014; 2015; 2016; Wang et al., 2015) as a criterion to estimate the

226 eddy forecast ability of the CSCASS. As fig. 5 shows, when the ANP is greater than 2

227 (that is the amplitude greater than 8 cm) AE2 can be well reproduced by the CSCASS.

228    Besides, we also use the independent evaluation, Fig.6 compared the assimilating

229 results of AE1 with the observations both from the satellite remote sensing and drifter

230 buoys trajectories of number 22517, 22918 and 22610 between December 3$^{rd}$ 2003 and

231 February 18$^{th}$ 2004. From Fig. 6 and Table 1, we can see that the generation and

232 movement of AE1 can be well reproduced by the CSCASS, with the pink curves

233 (assimilation) match well with those of black (satellite observations) and dotted lines

234 (the trajectories of drifter buoys). In addition, the spatial pattern of AE1 can also be well

235 revealed by the CSCASS: the meridional and zonal radii of AE1 detected by the

236 assimilation are 163 km and 93 km, which are almost equal to that of observations (148

237 km and 79 km). The migration path of AE1 can also be well reproduced by the CSCASS

238 (see Fig. 6, black and pink line) until its amplitude decays to less than 8 cm. In addition

239 to AE1, the generation and evolution of AE2 are also evaluated. As shown Fig. 7, the

240 evolution and propagation pathway of AE2 (Fig. 7b-7j), e.g. moving northwestward

241 firstly and then southwestward, can generally be reproduced by the CSCASS, although

242 its initial location shows a slight southward bias in the simulation (Fig. 7a). Similar to

243 the results of AE1, discrepancies between model and observations become larger again

244 during the decay phase of AE2.

245    In general, the comparison of assimilation SLA with that of satellite observation

246 and the trajectories of drifter buoys suggested that the generation, development and the

247 propagation of AE1 and AE2 can be reproduced by the CSCASS when their observed

248  amplitude greater than 8 cm (or the ANP greater than 2). However, when their

249  amplitudes are relatively small, less than 8 cm, the features of these two mesoscale

250  eddies are not well reproduced by the CSCASS. This may be related to the value setting

251  of parameter α, the localization length scale, and insufficient spatial resolution of

252  assimilated SSH or the numerical model (Counillon and Bertino, 2009).

253  **3.2 The predictability of these anticyclonic eddies in the NSCS**

254  Since the generation, development and the propagation of AE1 and AE2 can be

255  well reproduced by the CSCASS when their amplitude>8 cm (or the ANP greater than

256  2), as mentioned above, in this section we further use the CSCASS to investigate the

257  predictability of these two eddies. According to the generation, evolution and migration

258  of these two eddies, we designed six forecast experiments, hereafter referred to as Exp1

259  to Exp6 (see Fig.4) to investigate their predictability. The model's initial state prior to

260  each of the six forecast experiments is constrained by assimilating satellite SLA and

261  SST before. Based on the initial state, each experiment is run forward 30 days with the

262  forcing of 6-hourly wind, surface heat flux, and monthly mean river runoff, etc. The

263  first experiment, named Exp1, is applied on the 29$^{th}$ of November 2003, which tends to

264  study whether the generation of AE1 can be forecasted or not. Exp2 is implemented on

265  the 10$^{th}$ of December 2003 and is used to study whether the development and the

266  migration of AE1 can be forecasted. Exp3 is run based on the initial state on the 31$^{th}$ of

267  December 2003 and used to show whether the generation of AE2 and the continued

268  migration of AE1 can be forecasted. In order to investigate whether the continued

269  evolution of AE1 and AE2 can be forecasted, Exp4 is applied on the 21$^{th}$ of January

270    2004. Exp5, is setting up to reveal whether the attenuation of AE1 and the evolution of

271    AE2 can be forecasted, while Exp6 which is applied on the 29th of February 2004 was

272    designed to find out whether the disappearance of AE1 and AE2 can be forecasted.

273        The prediction results of Exp1 are shown in Fig. 8. In Fig. 8a, we can see that the

274    forecast is almost coincident with the satellite observation and the trajectory of drift

275    buoys, indicating that the generated position of AE1 can be well forecasted by the

276    CSCASS. In addition, the initial migration of AE1 can also be forecasted by the

277    CSCASS (see Fig. 8a and 8f). In order to evaluate the forecasted amplitude of AE1, the

278    amplitude and the distance of eddy centers between the observation and the forecast are

279    also quantified (Table 2: EXP1). From Table 2: EXP1, we can see that the amplitude of

280    forecasting matches well with that of observation, although its amplitude is slightly

281    larger than that of observation. After 4 weeks, the amplitude of the forecast is still close

282    to those of the observation, suggesting that the generation of AE1 can be well predicted

283    by the CSCASS.

284        In order to find out whether the development and movement path of AE1 can be

285    predicted after generation, we continue to carry out Exp2. As shown by the observation

286    (Fig. 9), AE1 moves southwestward along the continental shelf with its amplitude

287    decreasing and again increasing after its generation. This observed southwestward

288    movement is also predicted by the CSCASS (see pink closure curve in Fig. 9a-9d),

289    although a sudden southwestward movement cannot be well predicted (Fig. 9f). In

290    addition, the first attenuation and then enhancement of AE1 can also been predicted by

291    the CSCASS (see Table 2 and Fig. 9b). On the whole, the development and movement

path of AE1 can be well predicted by CSCASS for the first four weeks after its generation. After that, the errors between observation and prediction increase significantly, and by the fifth week, the distance between the center of the prediction and the observation become larger, more than 100 km (see Fig. 9e).

For further analysis, we carry out Exp3, to look at whether the continued evolution of AE1 and the generation of AE2 can be predicted. This experiment is carried out based on the initial condition of the assimilation on the 31$^{st}$ of December 2003 and the corresponding results are shown in Fig. 10 and Table 2. As shown by the prediction (Fig. 10, Table 2), although with a slightly weak amplitude, the CSCASS can reproduce AE1 after assimilating SLA and SST and predicted its development trend. In addition, the movement path of AE1 cannot be accurately predicted at this period, for instance, the observed AE1 moves directly to southwest (see red solid line and solid circle in Fig. 10f), but the predicted movement is firstly toward northeast, then turns to southwest (see blue solid line and solid circle in Fig. 10f). The generation of AE2 cannot be predicted in Exp3, which may be related to the smaller amplitude (<8 cm) of AE2 at this period.

The purpose of Exp4 is to look at whether the evolution of AE1 and AE2 can both be reasonably predicted. Since this experiment mainly focuses on the evolution of AE1 and AE2, thus Fig. 11 shows only the evolution of AE2 from the second week after generation, that is, from the beginning on the 21$^{st}$ of January 2004 to the fifth week. As shown in Fig. 11, Table 2 and Fig. 14d, the trends of amplitude variation of both eddies can be well predicted with the decreasing of AE1 and slow increasing of AE2. For AE1,

314 the results of the prediction and observation are very close in the first two weeks, with

315 the center of the two almost coincide. The central position of the prediction and

316 observation began to deviate after the third week. For AE2, although the amplitude and

317 movement path are not predicted well at its initial stage, the prediction is slowly

318 approaching to the observation during third to fifth week, and distance between the

319 center of the prediction and the observation is reduced from 132 km at the beginning to

320 81 km at the end (see Fig. 14d the black solid line).

321    As mentioned above, the purpose of Exp5 is to investigate whether the decay of

322 AE1 and the continued development of AE2 can be predicted. From Fig. 12, Table 2

323 and Fig. 14e, we can find that the CSCASS cannot predict the movement path of AE1

324 well in its decay stage: the distance between the center of the prediction and that of the

325 observation is greater than 188 km, and movement direction of the two is not consistent

326 (see red lines and dots in Fig. 12f). But the evolution and moving direction of AE2 can

327 be well predicted at this stage. The amplitude of observation and prediction of AE2 are

328 getting closer with time (Fig. 14e), although the speed of movement of AE2 given by

329 prediction is slower than that of observation (see blue dashed lines and hollow dots in

330 Fig. 12f).

331    The aim of Exp6 is to find whether the disappearance of AE1 and AE2 can be both

332 predicted. As described in Fig. 13, the disappearance of AE1 cannot be well predicted

333 owing to the low amplitude (less than 8 cm) of AE1 at this stage. Similarly, the

334 disappearance of AE2 is also less accurately predicted by the CSCASS (Fig. 14f). The

335 amplitude of AE2 from the observation decays continually at this stage, but the

336 amplitude of the predicted almost keeps constant. In addition, there is large deviation

337 of the direction of movement between prediction and observation for AE2 (see the red

338 solid line and dot in Fig. 13f).

339

340 **4. Conclusions and challenges for forecasting of mesoscale eddy**

341 In this paper, we carry out a series of assimilation and prediction experiments by

342 the CSCASS to assess the production and predictability of mesoscale eddies in the

343 NSCS, along with observations of satellite observed SST, SLA and the trajectory data

344 of drift. The comparisons of AE1 and AE2 observations with CSCASS prediction

345 experiments, which assimilate SLA and SST, show that when the amplitudes of

346 mesoscale eddy are higher than 8 cm, the generation, development, decay and

347 movement of eddies can be well reproduced, but when the amplitude of the mesoscale

348 eddy is lower than 8 cm, the generation and disappearance of mesoscale eddy cannot

349 be well reproduced.

350 The comparisons of AE1 and AE2 through six prediction experiments with

351 observations also show that the generation, evolution and movement path of these two

352 eddies with high amplitude (>8 cm or the ANP greater than 2) can be well predicted by

353 the CSCASS, although the generation mechanism of these two eddies is quite different

354 (Wang et al., 2008). However, when the amplitude of eddies becomes less than 8 cm,

355 the generation position and the movement path cannot be well predicted by the

356 CSCASS.

357 Our results suggested that for powerful mesoscale eddies, a good initial condition

358     after assimilating observations can help to improve their reproduction and predictability.

359     As mentioned above, the mesoscale eddies are related to strong nonlinear processes and

360     are not a deterministic response to atmospheric forcing, thus the quality of mesoscale

361     eddies forecast will depend primarily on the quality of the initial conditions. In addition,

362     the ability of the ocean numerical model to faithfully represent the ocean physics and

363     dynamics is also crucial. Although data assimilation, which combines observations with

364     the numerical model, can provide good initial conditions, it cannot make up for

365     limitations of numerical model algorithms and in its resolution. Hence for high-

366     resolution operational oceanography, numerical models need to be improved using

367     more accurate numerical algorithms and resolution especially in the weakly stratified

368     regions or on the continental shelf.

369     Furthermore, so far most of the information about the ocean variability is obtained

370     remotely from satellites (SSH and SST), the information about the subsurface

371     variability are very rare. Although a substantial source of subsurface data is provided

372     by the vertical profiles (i.e., expendable bathy thermographs, conductivity temperature

373     depth, and Argo floats), the datasets are still not sufficient to determine the state of the

374     ocean. In addition, in order to accurately assimilate the SSH anomalies from satellite

375     altimeter data into the numerical model, it is necessary to know the oceanic mean SSH

376     over the time period of the altimeter observations (Xu et al., 2011; Rio et al., 2014).

377     This is also a big challenge because the earth's geoid is not presented with sufficient

378     spatial resolution when assimilating SSH in an eddy-resolving model. With the advent

379     of the SWOT (Surface Water and Ocean Topography) satellite mission in 2020, it

380 should be possible to better resolve and forecast the mesoscale features in eddy

381 resolving ocean forecasting systems.

382

383 **Acknowledgements:**

384 This study is supported by the Marine Science and Technology Foundation of South

385 China Sea Branch, State Oceanic Administration (grant 1447), the National Key

386 Research and Development Program of China (2016YFC1401407), the Project of

387 Global Change and Air-Sea interaction under contract No. GASI-03-IPOVAI-04, the

388 National Natural Science Foundation of China (Grant No. 41731173, 41776037 and

389 41276027), and the China Scholarship Council (award to Xu Dazhi for 1 year's study

390 abroad at Nansen Environmental and Remote Sensing Center).

391

**References:**

393 Bleck, R.: An oceanic general circulation model framed in hybrid isopycnic cartesian

394   coordinates, Ocean Model., 4, 55-88, 2002.

395 Boyer, T. P., Levitus, S., Antonov, J. I., et al.: Linear trends in salinity for the World Ocean,

396   1955-1998, Geophy. Res. Lett., 32, 67-106, 2005.

397 Chassignet, E. P., Hurlburt, H. E., Smedstad, O. M., et al.: The HYCOM (Hybrid Coordinate

398   Ocean Model) data assimilative system, J. Mar. Sys., 65, 60-83, 2007.

399 Chelton, D. B., Schlax, M. G., and Samelson, R. M.: Global observations of nonlinear

400   mesoscale eddies, Progr. in Oceanogr., 91, 167-216, 2011.

401 Cheng, X. H., Qi, Y. Q., and Wang, W. Q.: Seasonal and Interannual Variabilities of Mesoscale

402   Eddies in South China Sea, J. Trop. Oceanogr., 24, 51-59, 2005.

403 Counillon, F., and Bertino, L.: Ensemble Optimal Interpolation: multivariate properties in the

404   Gulf of Mexico, Tellus, 61A, 296-308, 2009.

405 Dai, A., and Trenberth, K. E.: Estimates of freshwater discharge from continents: latitudinal

406   and seasonal variations, J. Hydrometeor., 3, 660-685, 2002.

407 Ducet, N., LeTraon, P. Y., and Reverdin, G.: Global high-resolution mapping of ocean

408   circulation from TOPEX/Poseidon and ERS-1 and-2, J. Geophy. Res., 105, 19477-19498,

409   2000.

410 Frenger, I., Gruber, N., Knutti, R., and Münnich, M.: Imprint of Southern Ocean eddies on

411   winds, clouds and rainfall, Nat. Geosci., 6, 608-612, 2013.

412 Fu, L.-L., Chelton, D. B., Traon, P.-Y. L., et al.: Eddy dynamics from satellite altimetry,

413   Oceanogr., 23, 14-25, 2010.

414 Halliwell, J. G. R.: Evaluation of vertical coordinate and vertical mixing algorithms in the

415   HYbrid-Coordinate Ocean Model (HYCOM), Ocean Model., 7, 285-322, 2004.

416 Halliwell, J. G. R., Bleck, R., and Chassignet, E. P.: Atlantic Ocean simulations performed using

417   a new Hybrid Coordinate Ocean Model (HYCOM), EOS, Fall AGU Meeting, 1998.

418 Halliwell, J. G. R., Bleck, R., Chassignet, E. P., et al.: Mixed layer model validation in Atlantic

419   Ocean simulations using the Hybrid Coordinate Ocean Model (HYCOM), EOS, 80,

420    OS304, 2000.

421    Hamilton, P., Fargion, G. S., and Biggs, D. C.: Loop Current eddy paths in the western Gulf of

422        Mexico, J. Phys. Oceanogr., 29, 1180-1207, 1999.

423    Han, Y.–J.: A numerical world ocean general circulation model: Part II. A baroclinic experiment,

424        Dyn. Atmos. Oceans, 8,141-172, 1984.

425    Huang, B. Q., Hua, J., Xu, H. Z., et al.: Phytoplankton community at warm eddies in the

426        northern South China Sea in winter 2003/2004, Deep Sea Res. Part II, 57, 1792-1798,

427        2010.

428    Jia, Y., Liu, Q., and Liu, W.: Primary studies of the mechanism of eddy shedding from the

429        Kuroshio bend in Luzon Strait, J. Oceanogr., 61, 1017-1027, 2005.

430    Kara, A. B., Rochford, P. A., and Hurlburt H E.: Air-sea flux estimates and the 1997-1998

431        ENSO event, Boundary-Layer Meteorol., 103, 439-458, 2002.

432    Large, W. G., McWilliams, J. C., and Doney, S. C.: Oceanic vertical mixing: a review and a

433        model with a nonlocal boundary layer parameterization, Rev. Geophys., 32, 363-403,

434        1994.

435    Legates, D. R., and Willmott, C. J.: Mean seasonal and spatial variability in gauge-corrected,

436        global precipitation, Int. J. Climatol., 10, 111-127, 1990.

437    Li, L., Nowlin, W. D., and Su, J, L.: Anticyclonic rings from the Kuroshio in the South China

438        Sea, Deep-Sea Res., Part I, 45, 1469-1482, 1998.

439    Li, Q. Y., and Sun, L.: Technical Note: Watershed strategy for oceanic mesoscale eddy splitting,

440        Ocean Sci., 11, 269-273, doi:10.5194/os-11-269-2015, 2015.

441    Li, Q. Y., Sun, L., and Lin, S.-F.: GEM: a dynamic tracking model for mesoscale eddies in the

442        ocean, Ocean Sci., 12, 1249-1267, doi:10.5194/os-12-1249-2016, 2016.

443    Li, Q. Y., Sun, L., Liu, S.-S., et al.: A new mononuclear eddy identification method with simple

444        splitting strategies, Remote Sens. Lett., 5, 65-72. Doi:10.1080/2150704X.2013.872814,

445        2014.

446    Li, X. C.: Applying a new localization optimal interpolation assimilation module to assimilate

447        sea surface temperature and sea level anomaly into the Chinese Shelf/Coastal Seas model

448        and carry out hindcasted experiment, Graduate University of the Chinese Academy of

449        Sciences, China, 92 pp, 2009.

450  Li, X. C., Zhu, J., Xiao, Y. G., et al.: A Model-Based Observation Thinning Scheme for the

451      Assimilation of High-Resolution SST in the Shelf and Coastal Seas around China, J.

452      Atmos. Oceanic Technol., 27, 1044-1058, 2010.

453  Liu, Z., Yang, H. J., and Liu, Q.: Regional dynamics of seasonal variability of sea surface height

454      in the South China Sea, J. Phys. Oceanogr., 31, 272-284, 2001.

455  Morrow, R., and Traon, P.-Y. L.: Recent advances in observing mesoscale ocean dynamics with

456      satellite altimetry, Adv. Spa. Res., 50, 1062-1076, 2012.

457  Oey, L. T., Ezer, T., and Lee, H. C.: Loop Current, rings and related circulation in the Gulf of

458      Mexico: a review of numerical models. In: Circulation in the Gulf of Mexico:

459      Observations and Models Volume 161, American Geophysical Union, 31-56, 2005.

460  Oke, P. R., Allen, J. S., Miller, R. N., et al.: Assimilation of surface velocity data into a primitive

461      equation coastal ocean model, J. Geophy. Res. Oceans, 107, 5-1-5-25, 2002.

462  Oke, P. R., Brassington, G. B., Griffin, D. A., et al.: Ocean data assimilation: a case for ensemble

463      optimal interpolation, Australian Meteorological and Oceanographic Journal, 59, 67-76,

464      2010.

465  Reynolds, R. W., Smith, T. M., Liu, C., et al.: Daily High-Resolution Blended Analyses for Sea

466      Surface Temperature, J. Climate, 20, 5473-5496, 2007.

467  Rio, M. H., Mulet, S., and Picot, N.: Beyond GOCE for the ocean circulation estimate:

468      Synergetic use of altimetry, gravimetry, and in situ data provides new insight into

469      geostrophic and Ekman currents, Geophy. Res. Lett., 41, 8918-8925, 2014.

470  Treguier, A. M., Chassignet, E. P., Boyer, A. L., et al.: Modeling and forecasting the "weather

471      of the ocean" at the mesoscale, J. Mar. Res., 75, 301-329, 2017.

472  Uppala, S., Kallberg, P., Simmons, A. J., et al.: The EAR-40 re-analysis, Q. J. R. Meteorol. Soc.,

473      131, 2961-3012, 2005.

474  Vos, M. D., Backeberg, B., and Counillon, F.: Using an eddy-tracking algorithm to understand

475      the impact of assimilating altimetry data on the eddy characteristics of the Agulhas system,

476      Ocean Dyn., 1-21, 2018.

477  Wang, D. X., Zhou, F. Z., and Qin Z. H.: Numerical simulation of the upper ocean circulation

478      with two-layer model, Acta Oceanol. Sin., 18, 30-40, 1996.

479  Wang, D., Xu, H., Lin, J., et al.: Anticyclonic eddies in the northeastern South China Sea during

winter 2003/2004, J, Oceanogr., 64, 925-935, doi: 910.1007/s10872-10008-10076-10873, 2008.

Wang, G., Su, J., and Chu, P. C.: Mesoscale eddies in the South China Sea observed with altimeter data, Geophy. Res. Lett., 30, 2121, doi: 10.1029/2003GL018532, 2003.

Wang, Z., Li, Q., Sun, L., Li, S., et al.: The most typical shape of oceanic mesoscale eddies from global satellite sea level observations, Front. Earth Sci., 9, 202-208. DOI 10.1007/s11707-014-0478-z, 2015.

Woodham, R. H., Alves, O., Brassington, G. B., et al.: Evaluation of ocean forecast performance for Royal Australian Navy exercise areas in the Tasman Sea, J. Oper. Oceanogr., 8, 147-161, 2015.

Woodruff, S. D., Slutz, R. J., Jenne, R. L., et al.: A comprehensive ocean-atmosphere data set, Bull. Am. Meteorol. Soc., 68, 1239-1250, 1987.

Wu, C. R., and Chiang, T. L.: Mesoscale eddies in the northern South China Sea, Deep-Sea Res., Part II, 54, 1575-1588, 2007.

Xiao, X. J., Wang, D. X., and Xu, J.-J.: The assimilation experiment in the southwestern South China Sea in summer 2000, Chin. Sci. Bull., 51, 31-37, 2006.

Xie, J. P., Bertino, L., Cardellach, E., et al.: An OSSE evaluation of the GNSS-R altimetery data for the GEROS-ISS mission as a complement to the existing observational networks, Remote Sens. Environ., 209, 152-165, 2018.

Xie, J. P., Counillon, F., Zhu, J., et al.: An eddy resolving tidal-driven model of the South China Sea assimilating along-track SLA data using the EnOI, Ocean Sci., 8, 609-627, 2011.

Xu, D. Z., Li, X. C., Zhu, J., et al.: Evaluation of an ocean data assimilation system in the marginal seas around China, with a focus on the South China Sea, Chin. J. Oceanol. Limnol., 29, 414-426, 2011.

Xu, D. Z., Zhu, J., Qi, Y. Q., et al.: Impact of mean dynamic topography on SLA assimilation in an eddy-resolving model, Acta Oceanol. Sin., 31, 11-25, 2012.

Yan, C. X., Zhu, J., and Zhou, G. Q.: Impacts of XBT, TAO, altimetry and ARGO observations on the tropic Pacific Ocean data assimilation, Adv. Atmos. Sci., 24, 383-398, 2007.

Yang, K., Shi, P., Wang, D. X., et al.: Numerical study about the mesoscale multi-eddy system in the northern South China Sea in winter, Acta Oceanol. Sin., 22, 27-34, 2000.

510 Yang, S., Xing, J., Chen, D., et al.: A modelling study of eddy-splitting by an island/seamount,

511 Ocean Sci., 13, 837-849, https://doi.org/10.5194/os-13-837-2017, 2017.

512 Zhai, X., Johnson, H. L., Marshall, D. P.: Significant sink of ocean-eddy energy near western

513 boundaries. Nat. Geosci., 3, 608-612, 2010.

514 Zhu, J.: Overview of Regional and Coastal Systems, Chapter 17 in Operational Oceanography

515 in the 21st Century. Edited by A. Schiller and G. B. Brassington, PP. 727, Springer Science,

516 Business Media B.V, 2011.

517 Zhuang, W., Du, Y., Wang, D. X., et al.: Pathways of mesoscale variability in the South China

518 Sea, Chin. J. Oceanol. Limnol., 28, 1055-1067, 2010.

519

520 **Figures:**

521
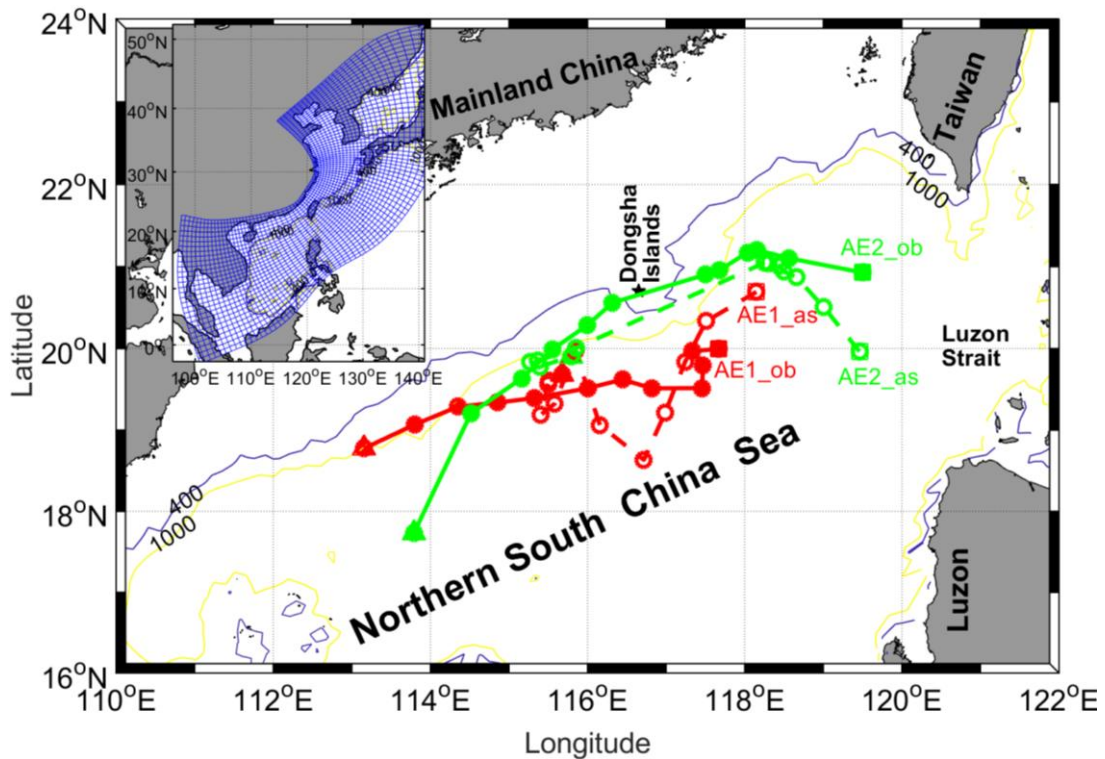
522

523 Fig. 1 Bathymetry of the northern South China Sea. The blue and yellow contour lines are the

524 isolines of 400 m and 1000 m. The solid black Pentagram indicated Dongsha Islands. The migration

525 path of AE1 and AE2 in the NSCS during December 2003~April 2004. Red solid (hollow) circle

526 dots and solid (dash) lines indicated weekly passing position and migration path of observation

527 (assimilation) AE1. Green solid (hollow) circle dots and solid (dash) lines indicated weekly passing

528 position and migration path of observation (assimilation) AE2. The quadrangle and triangle denoted

529 start and end position, respectively. The model domain of CSCSS (the inset panel), the curvilinear

530 orthogonal model grid with 1/8-1/12° horizontal resolution (147×430) is denoted by the blue grid

531 (at intervals of 10 grid cells here).

532

533

534
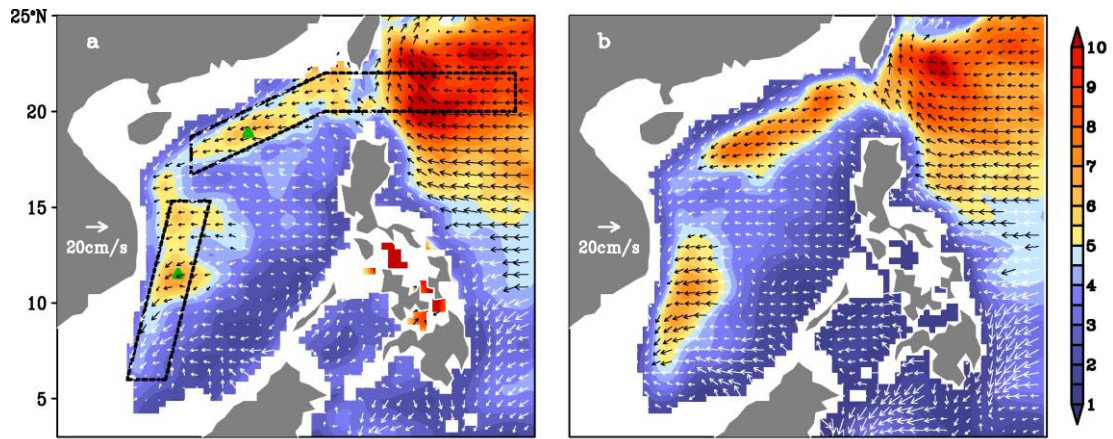
Fig. 2 Annual mean standard deviation of sea level mesoscale signals (color shading, unit: cm) and propagation velocities of the signals (vectors) derived from (a) altimeter observations; (b) OFES simulations. From Zhuang et al. (2010).

538

539
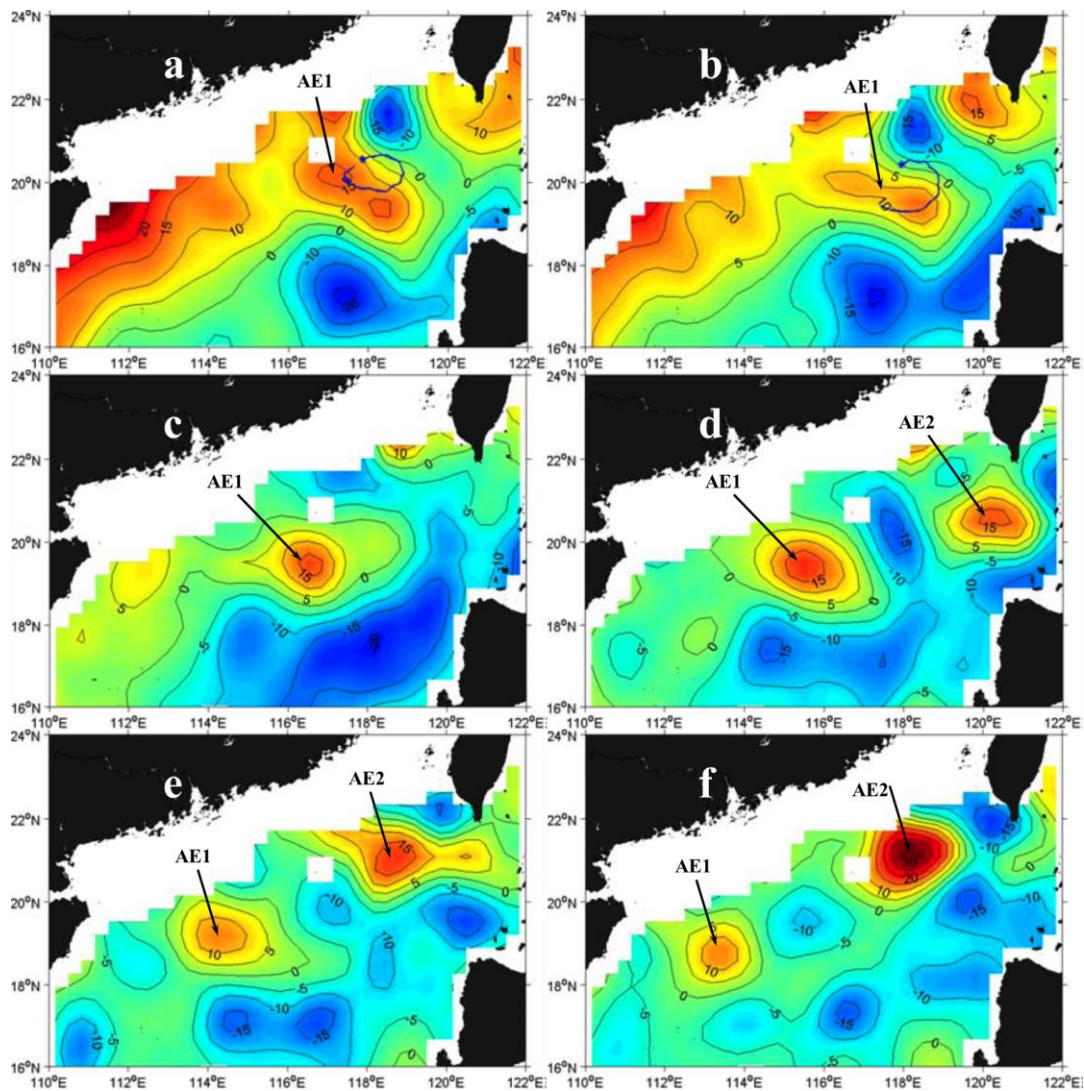
Fig. 3 Snapshots of SLA from satellite remote sensing datasets. Buoy 22918 trajectory (blue lines,

blue asterisk represents the initial position of buoy, as in Fig. 4) (a) from December 4-15, 2003

superposed on SLA field on December 10, 2003; (b) from December 16-23, 2003 superposed on

SLA field on December 17, 2003; SLA field on (c) January 7, 2004; (d) January 21, 2004; (e)

February 4, 2004; (f) February 18, 2004.   From Wang et al. (2008).
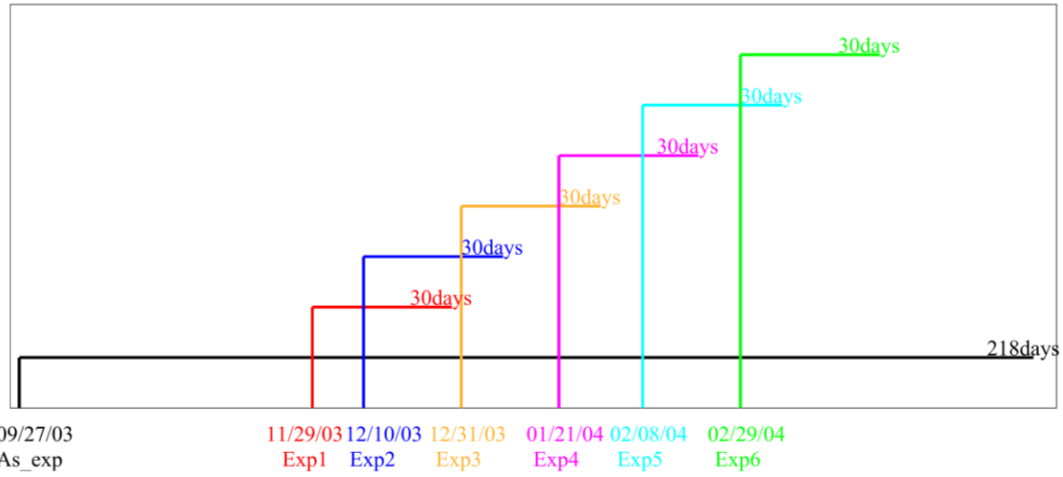
Fig. 4 The settings of assimilation and six forecast experiments, including the start and end date.
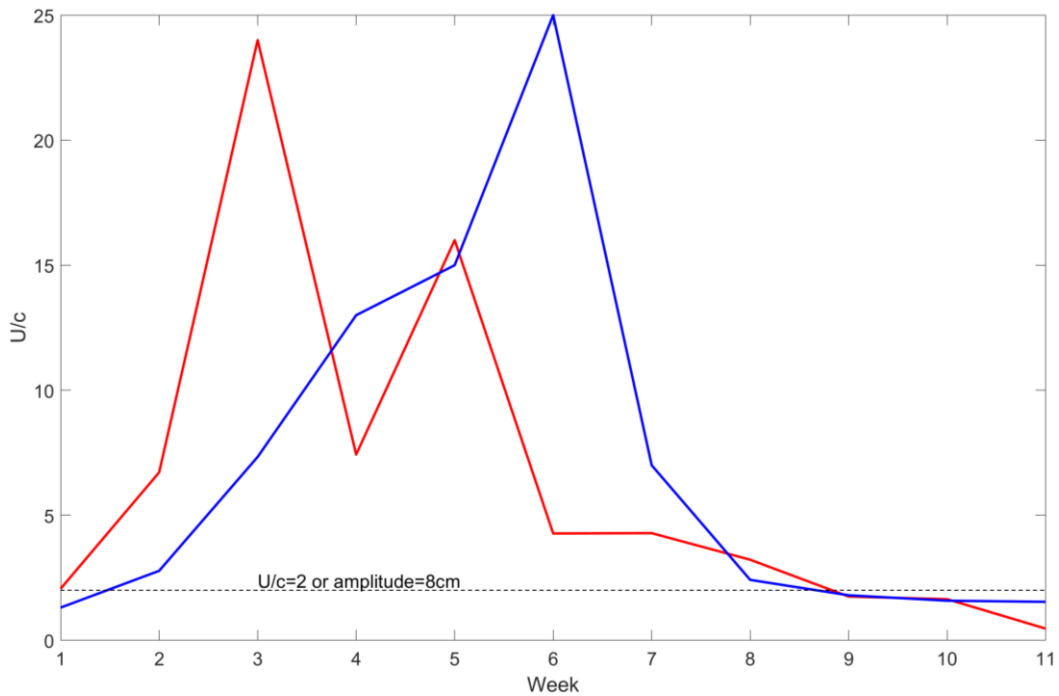
Fig. 5 The advective nonlinearity parameter U/c (ANP). The thick red (blue) curve indicates the
ANP of the observed (As_exp experiment) of AE2, the dash line indicates the value of eddy
amplitude at 8 cm or the ANP greater than 2.
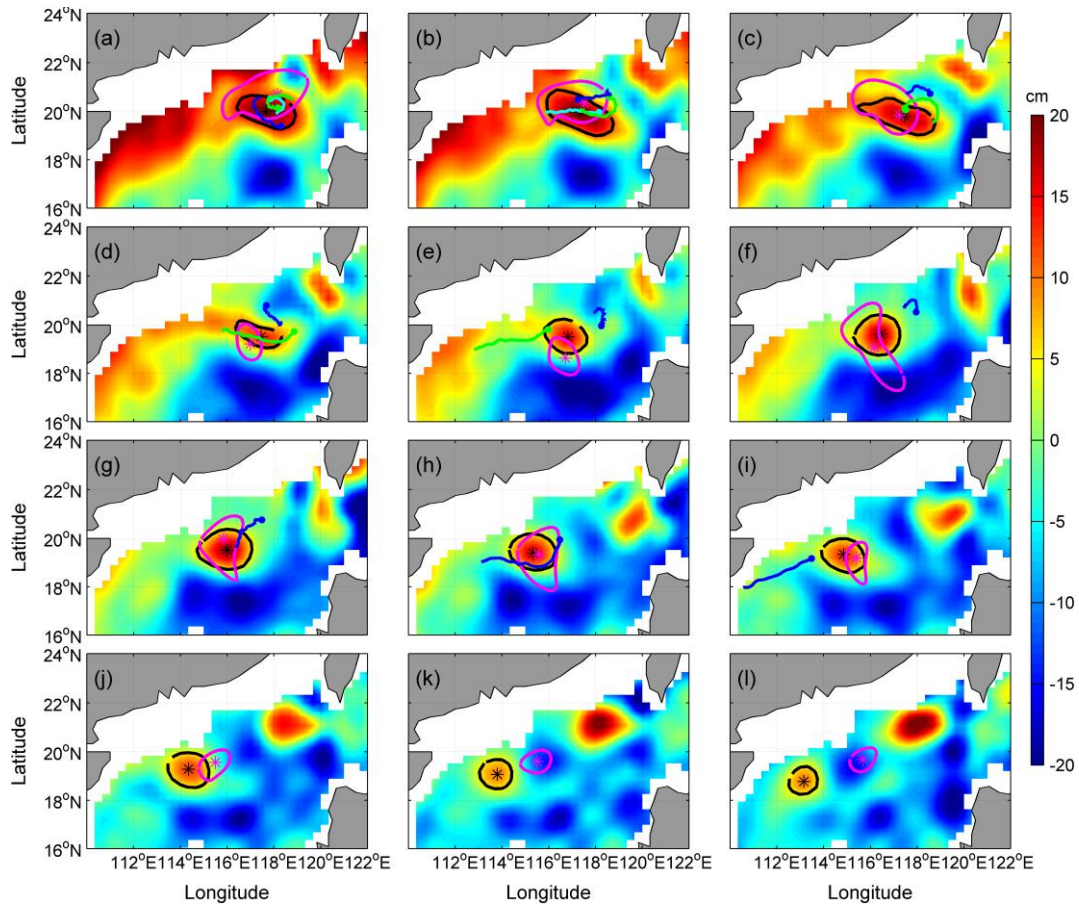
553

554 Fig. 6 Comparisons of AE1 derived from weekly SLA of assimilation results and observation from

555 satellite remote sensing during the period of December 2003~February 2004. Background color is

556 SLA, "*" mark and closed lines indicated the center position and the outermost closed isoline of

557 AE1, respectively, the black is from satellite observation SLA, the pink is from assimilation SLA.

558 The cyan, green and blue solid circle lines indicated the start positions and trajectories of number

559 22517, 22918 and 22610 drifter buoys, respectively. (a)-(l) is SLA on the 3rd of December 2003~

560 the 18th of February 2004, respectively. Unit: cm.
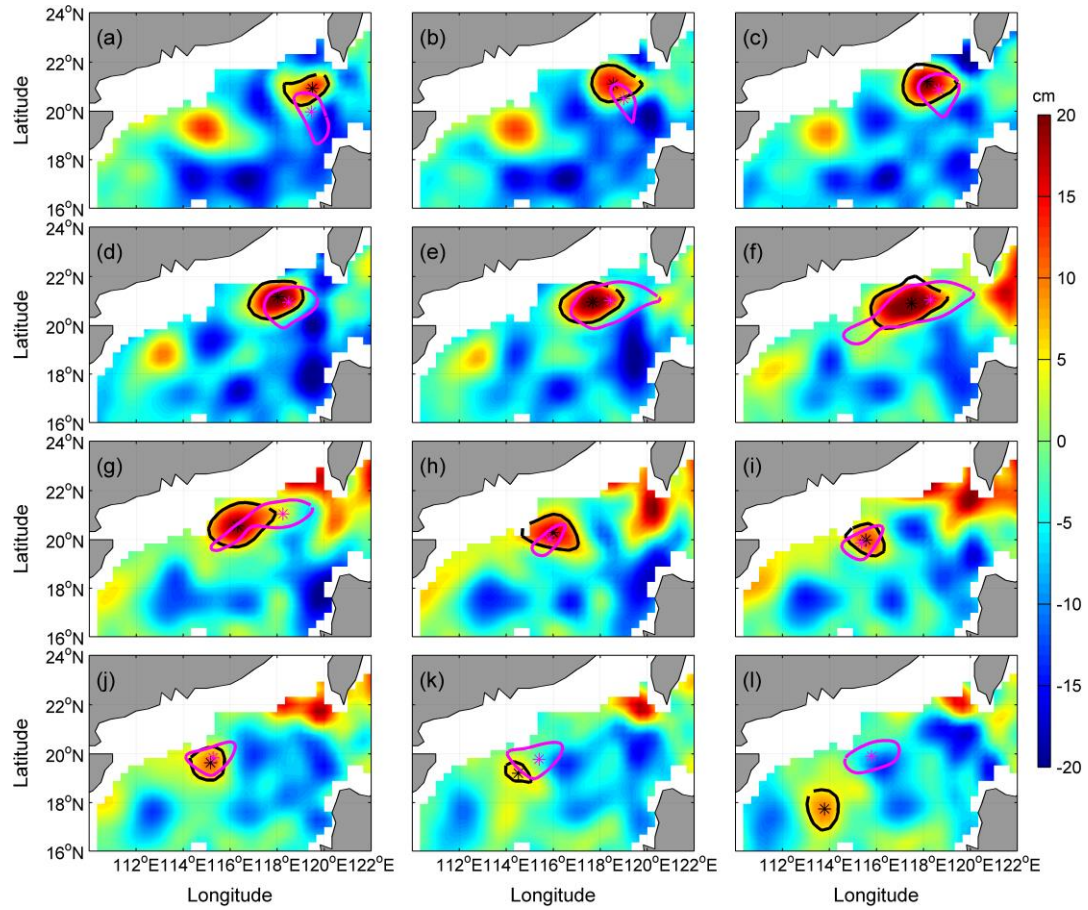
561

562    Fig. 7 The same as figure 4, But for AE2, the corresponding period is January 28<sup>th</sup>, 2003~April 14<sup>th</sup>, 20

563

564

565

566

567 **Tables:**

568

569

570 Table 1 The amplitude of AE1 and AE2 derived from observation SLA and the assimilation SLA, and distance of eddy centers between the observation SLA's and

571 assimilation SLA's.

| Weekly | | | 1(2003/12/3) | 2 | 3 | 4 | 5 | 6 | 7 | 8 | 9 | 10 | 11 | 12 |
|---|---|---|---|---|---|---|---|---|---|---|---|---|---|---|
| AE1 | Distance (km) | | 94 | 45 | 26 | 62 | 98 | 70 | 54 | 30 | 63 | 131 | 199 | 298 |
| | Amplitude(cm) | Observed | 8 | 10 | 9 | 8 | 8 | 13 | 13 | 11 | 8 | 8 | 4 | 6 |
| | | Assimilated | 18 | 12 | 11 | 6 | 5 | 4 | 5 | 6 | 2 | 3 | 3 | 2 |
| Weekly | | | 1(2004/1/28) | 2 | 3 | 4 | 5 | 6 | 7 | 8 | 9 | 10 | 11 | 12 |
| AE2 | Distance (km) | | 107 | 83 | 67 | 57 | 85 | 91 | 221 | 36 | 26 | 26 | 117 | 328 |
| | Amplitude(cm) | Observed | 7 | 12 | 18 | 17 | 17 | 16 | 15 | 10 | 7 | 6 | N/A | 6 |
| | | Assimilated | 3 | 2 | 5 | 6 | 10 | 8 | 4 | 8 | 9 | 4 | 5 | 6 |

572

573

574

575 Table 2 The amplitude of AE1 and AE2 derived from observation SLA and the six forecast SLA,

576 and distance of eddy centers between the observation SLA's and forecast SLA's.

| Weekly | | | | 1 | 2 | 3 | 4 | 5 |
|---|---|---|---|---|---|---|---|---|
| Exp1 | Distance (km) | | | 80 | 58 | 32 | 68 | 47 |
| | Amplitude (cm) | Observed | | 8 | 10 | 9 | 8 | 8 |
| | | Forecasted | | 14 | 12 | 14 | 11 | 12 |
| Exp2 | Distance (km) | | | 57 | 22 | 63 | 51 | 113 |
| | Amplitude (cm) | Observed | | 10 | 9 | 8 | 8 | 13 |
| | | Forecasted | | 12 | 11 | 6 | 8 | 10 |
| Exp3 | Distance (km) | | | 134 | 85 | 111 | 130 | 124 |
| | Amplitude (cm) | Observed | | 13 | 13 | 11 | 8 | 8 |
| | | Forecasted | | 2 | 3 | 3 | 3 | N/A |
| Exp4 | AE1 | Distance (km) | | 32 | 58 | 111 | 161 | 231 |
| | | Amplitude (cm) | Observed | 11 | 8 | 8 | 4 | 6 |
| | | | Forecasted | 4 | 2 | 2 | 2 | N/A |
| | AE2 | Distance (km) | | N/A | N/A | 132 | 95 | 81 |
| | | Amplitude (cm) | Observed | N/A | N/A | 12 | 18 | 17 |
| | | | Forecasted | N/A | N/A | N/A | 6 | 9 |
| Exp5 | AE1 | Distance (km) | | 188 | 274 | 287 | 405 | 503 |
| | | Amplitude (cm) | Observed | 4 | 6 | 2 | N/A | N/A |
| | | | Forecasted | 2 | 2 | 2 | 2 | 2 |
| | AE2 | Distance (km) | | 69 | 77 | 102 | 95 | 226 |
| | | Amplitude (cm) | Observed | 18 | 17 | 17 | 16 | 15 |
| | | | Forecasted | 5 | 7 | 6 | 6 | 9 |
| Exp6 | AE2 | Distance (km) | | 91 | 227 | 277 | 339 | 453 |
| | | Amplitude (cm) | Observed | 16 | 15 | 10 | 7 | 6 |
| | | | Forecasted | 7 | 9 | 6 | 4 | 6 |

577
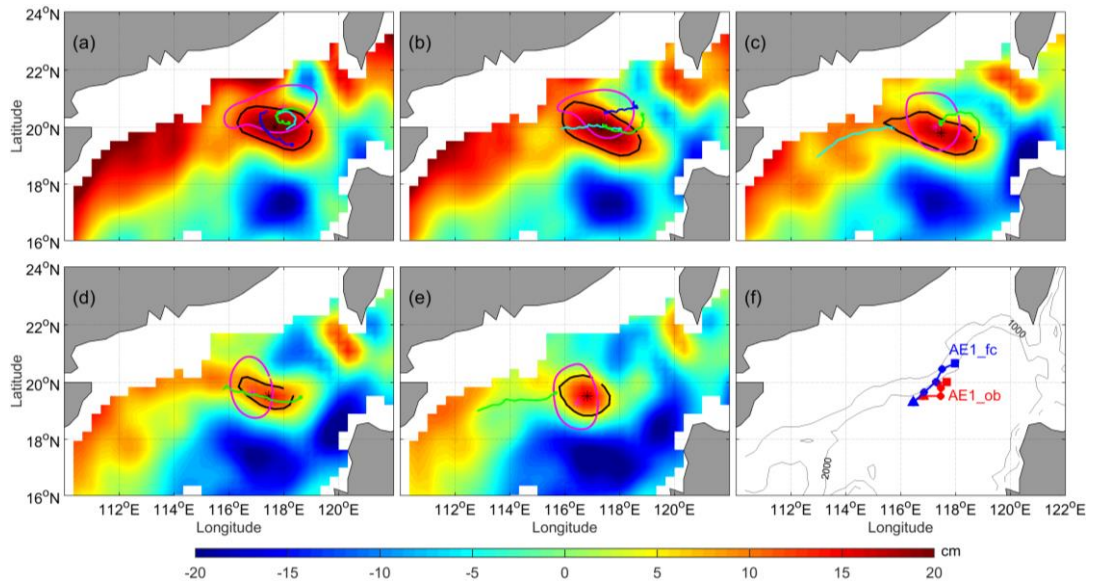
Fig. 8 Comparison of AE1 of Exp1 and observation, and trajectories of drifter buoys during the 29th of November 2003 and the 29th of December 2004. The cyan, green and blue solid circle dots and lines indicated the start positions and trajectories of number 22917, 22918 and 22610 drift buoys during the corresponding period, respectively. Where, the red (blue) dotted line in (f) is the moving path of AE1 derived from observation (forecast) SLA during the experiment period, the square (triangle) represents the start (end) position.
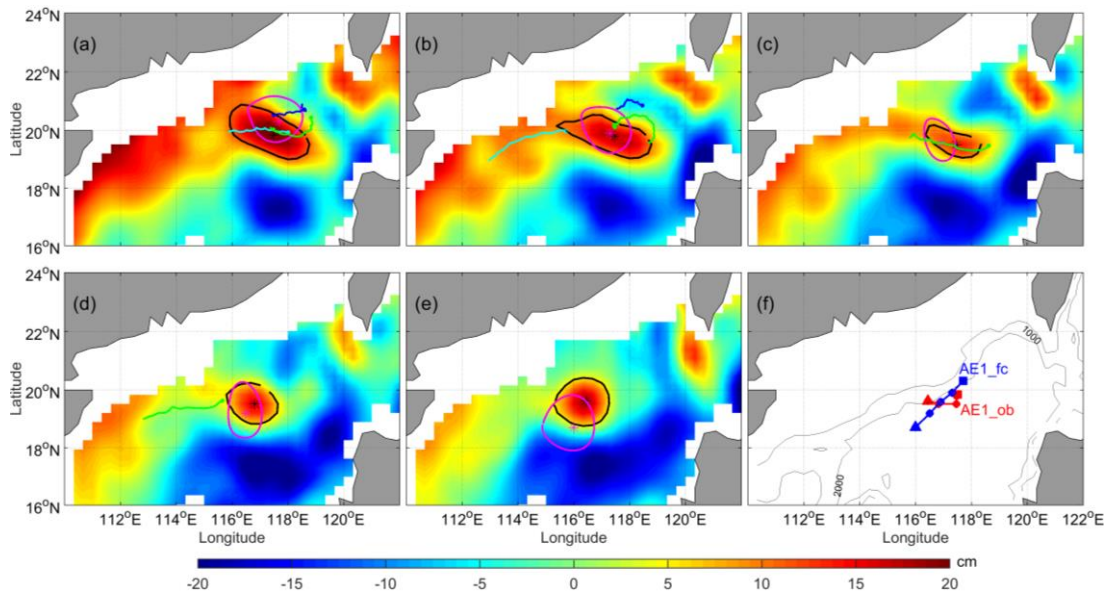
Fig. 9 Same as figure 8, but for Exp2, the experiment period is the 10th of December 2003 to the 9th of January 2004.
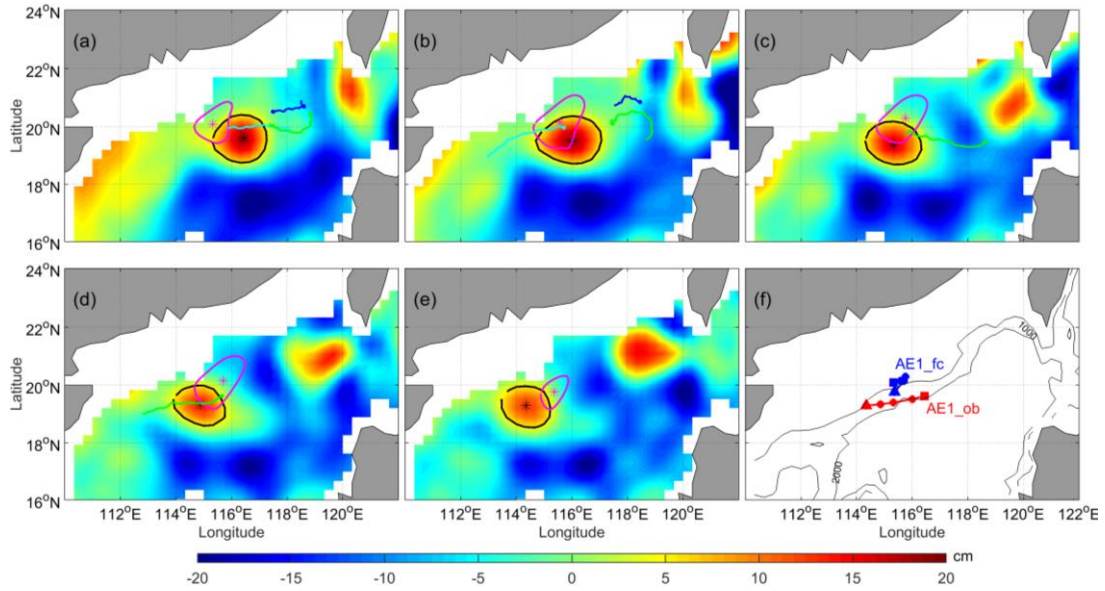
Fig. 10 Same as figure 9, but for Exp3, the experiment period is the 31st of December 2003 to the 30th of January 2004.
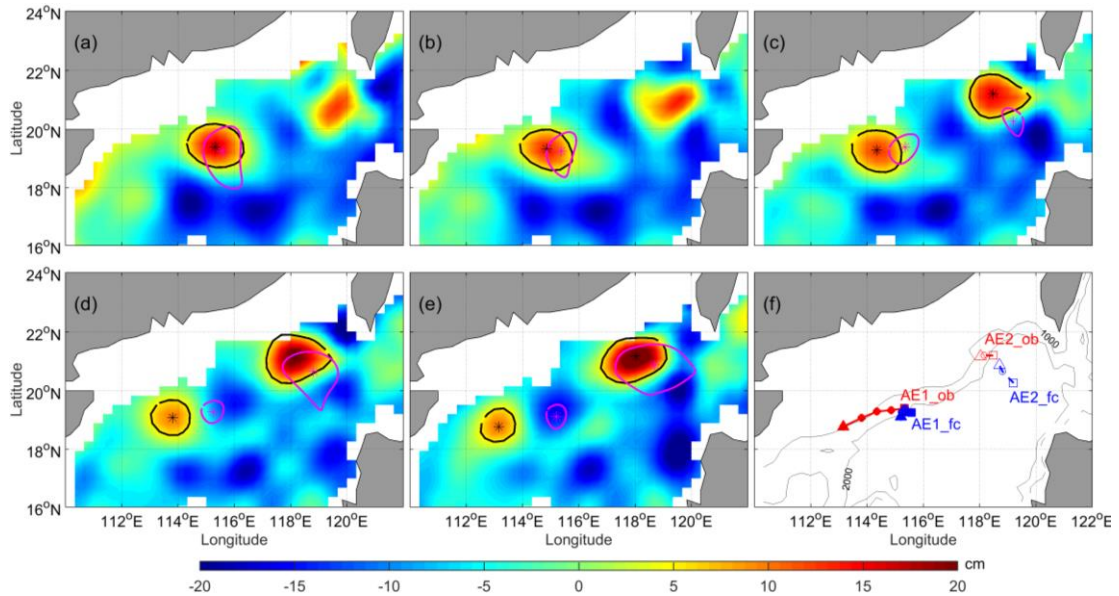
Fig. 11 Same as figure 8, but for Exp4,where, the red (blue) dotted line in (f) is the observation (forecast) moving path of AE1 and AE2. the red solid (dashed) lines and solid (hollow) circle derived from observation SLA for AE1 (AE2), the blue solid (dashed) lines and solid (hollow) circle derived from forecast SLA during the 21st of January 2004 to the 20th of February 2004.
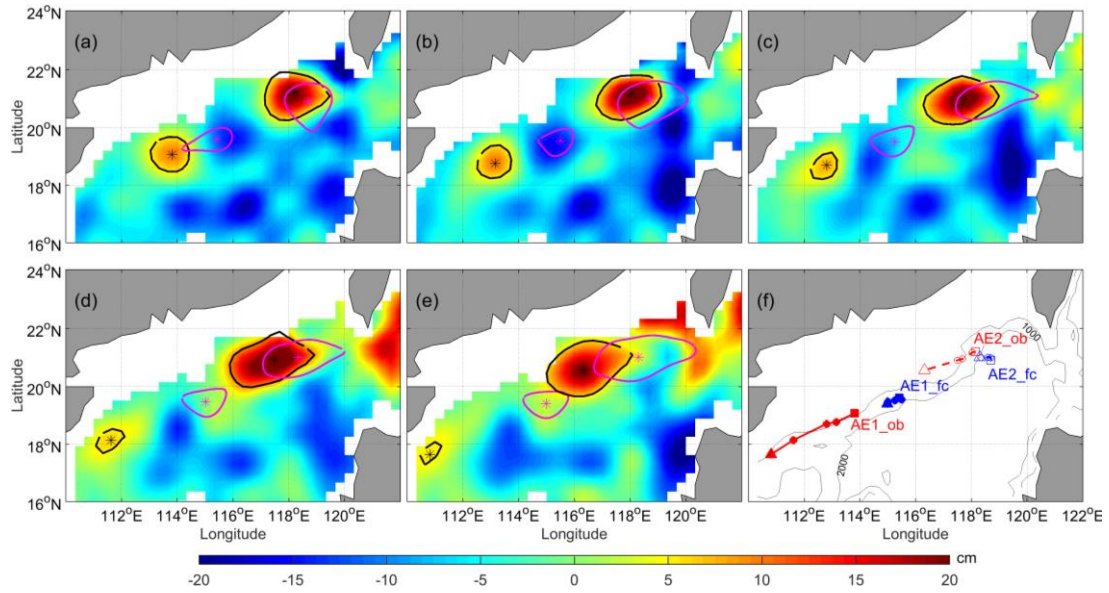
Fig. 12 Same as figure 11, but for Exp5, the experiment period is the 8th of February 2004 to the 10th of March 2004.
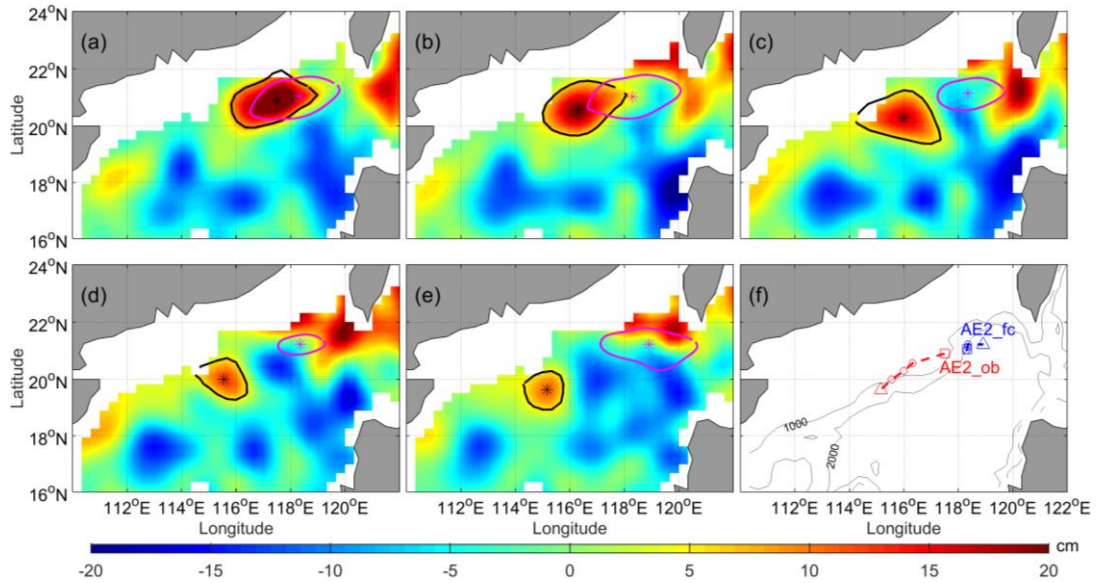
Fig. 13 Same as figure 11, but for Exp6 and AE2, the experiment period is the 29th of February 2004 to the 30th of March 2004.
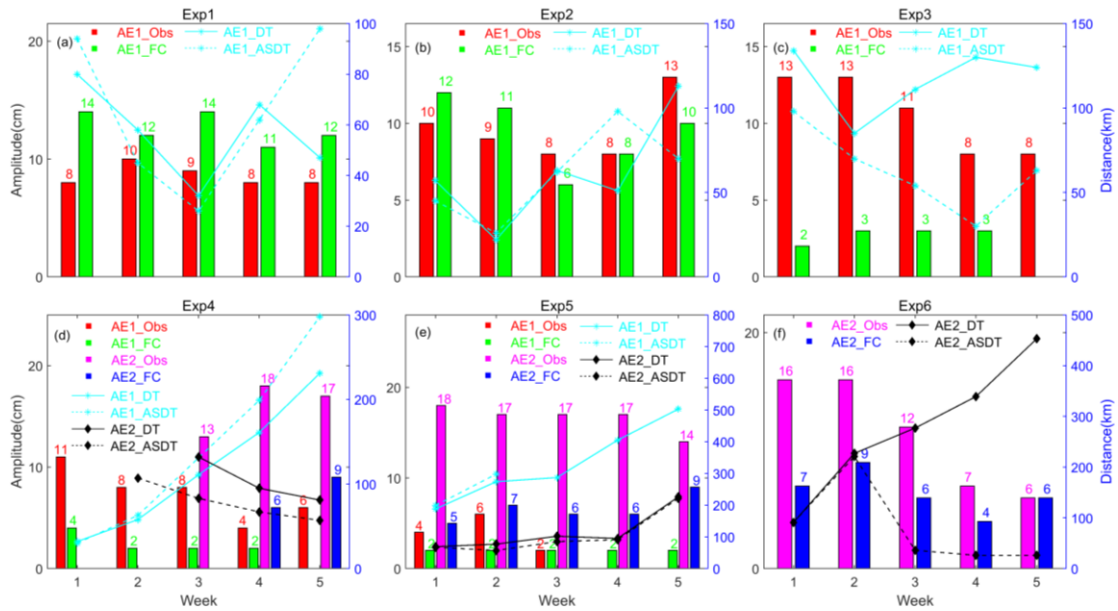
Fig. 14 The amplitude of AE1 and AE2 derived from observation SLA and the six forecast SLA, and distance of eddy centers between the observation, assimilation and forecast SLA's, respectively. The red and green histograms indicated the AE1 amplitudes from observation and prediction respectively. The pink and blue histograms expressed the AE2 amplitudes from observation and prediction respectively. The cyan star solid (dash) line shows the distance of the center between observation and prediction (assimilation) AE1. The black diamond solid (dash) line shows the distance of the center between observation and prediction (assimilation) AE2.